Remote Sensing of Environment 223 (2019) 179–193

Contents lists available at ScienceDirect

Remote Sensing of Environment

journal homepage: www.elsevier.com/locate/rse

Gradients in urban material composition: A new concept to map cities with spaceborne imaging spectroscopy data*

Marianne Jilge[a,b,*], Uta Heiden[b], Carsten Neumann[c], Hannes Feilhauer[d,e]

[a] Ruhr-University Bochum, Geomatics/Remote Sensing Group, Geography Department, Universitätsstraße 150, 44780 Bochum, Germany
[b] German Aerospace Center (DLR), German Remote Sensing Data Center (DFD), Oberpfaffenhofen, 82234 Wessling, Germany
[c] German Research Centre for Geosciences (GFZ), Telegrafenberg, 14473 Potsdam, Germany
[d] Friedrich-Alexander-Universität Erlangen-Nürnberg, Institute of Geography, Wetterkreuz 15, 91058 Erlangen, Germany
[e] Freie Universität Berlin, Institute of Geographical Sciences, Malteserstraße 74-100, 12249 Berlin, Germany

ARTICLE INFO

Keywords:
EnMAP
Gradient analysis
Imaging spectroscopy
Urban
Surface materials

ABSTRACT

To understand processes in urban environments, such as urban energy fluxes or surface temperature patterns, it is important to map urban surface materials. Airborne imaging spectroscopy data have been successfully used to identify urban surface materials mainly based on unmixing algorithms. Upcoming spaceborne Imaging Spectrometers (IS), such as the Environmental Mapping and Analysis Program (EnMAP), will reduce the time and cost-critical limitations of airborne systems for Earth Observation (EO). However, the spatial resolution of all operated and planned IS in space will not be higher than 20 to 30 m and, thus, the detection of pure Endmember (EM) candidates in urban areas, a requirement for spectral unmixing, is very limited. Gradient analysis could be an alternative method for retrieving urban surface material compositions in pixels from spaceborne IS. The gradient concept is well known in ecology to identify plant species assemblages formed by similar environmental conditions but has never been tested for urban materials. However, urban areas also contain neighbourhoods with similar physical, compositional and structural characteristics. Based on this assumption, this study investigated (1) whether cover fractions of surface materials change gradually in urban areas and (2) whether these gradients can be adequately mapped and interpreted using imaging spectroscopy data (e.g. EnMAP) with 30 m spatial resolution.

Similarities of material compositions were analysed on the basis of 153 systematically distributed samples on a detailed surface material map using Detrended Correspondence Analysis (DCA). Determined gradient scores for the first two gradients were regressed against the corresponding mean reflectance of simulated EnMAP spectra using Partial Least Square regression models. Results show strong correlations with $R^2 = 0.85$ and $R^2 = 0.71$ and an RMSE of 0.24 and 0.21 for the first and second axis, respectively. The subsequent mapping of the first gradient reveals patterns that correspond to the transition from predominantly vegetation classes to the dominance of artificial materials. Patterns resulting from the second gradient are associated with surface material compositions that are related to finer structural differences in urban structures. The composite gradient map shows patterns of common surface material compositions that can be related to urban land use classes such as Urban Structure Types (UST). By linking the knowledge of typical material compositions with urban structures, gradient analysis seems to be a powerful tool to map characteristic material compositions in 30 m imaging spectroscopy data of urban areas.

1. Introduction

More than 54% of the world's population is currently residing in cities. This percentage will continue to increase in the future (UN, 2014), leading to an urgent and growing demand for detailed and spatially explicit information about urban areas. Chen et al. (2012) discuss the detailed information of surface materials needed for urban weather and climate modelling and specify the requirements to better describe urban canopy models. These models are based on information about the spatial configuration of urban areas and about the surface materials of urban objects that drive surface-atmosphere exchange processes (e.g. Shashua-Bar et al., 2004; Taleghani et al., 2015; Bruse

* Please refer to the online version of the article for a representation in colour.

* Corresponding author at: German Aerospace Center (DLR), German Remote Sensing Data Center (DFD), Oberpfaffenhofen, 82234 Wessling, Germany.
E-mail address: marianne.jilge@dlr.de (M. Jilge).

https://doi.org/10.1016/j.rse.2019.01.007
Received 5 June 2018; Received in revised form 12 December 2018; Accepted 8 January 2019
Available online 26 January 2019

and Fleer, 1998). Knowledge gained from such model simulations can be used to measure and understand the impacts of climate change on urban areas. Since these impacts affect the urban population locally (Grimm et al., 2008), urban planning focuses on the transformation of cities in response to the changing climate and to develop adaptation responses in advance (Carter et al., 2015).

A wide range of airborne and spaceborne Earth Observation missions have previously been used to study details of urban structures (Voltersen et al., 2014; Cai et al., 2017), urban growth (Esch et al., 2017; Pesaresi et al., 2016; Bagan and Yamagata, 2012; Herold et al., 2003) and ecological functions of urban areas (Lakes and Kim, 2012; Alberti, 2005; Alonzo et al., 2016). With the wider availability of airborne imaging spectrometers, studies have been expanded to map and quantify surface material composition in urban areas (Roessner et al., 2001; Heiden et al., 2007; Heiden et al., 2012; Okujeni et al., 2013; Priem and Canters, 2016; Segl et al., 2003; Franke et al., 2009; Demarchi et al., 2014). The main advantage of using imaging spectroscopy data is the rich spectral information content that enables a detailed surface material inventory.

However, airborne imaging spectroscopy data have limited availability and are cost-intensive and, thus, not applicable for frequent monitoring of cities. These limitations can be overcome with spaceborne imaging spectrometers, although studies are still rare due to the limited availability of sensor data. There are a few urban studies using spaceborne imaging spectroscopy data from former and operating sensors, such as Hyperion on EO-1 (Cavalli et al., 2008; Fan and Deng, 2014; Weng and Lu, 2008; Weng et al., 2008; Xu and Gong, 2007; Zhang, 2016) and CHRIS on the PROBA platform (Demarchi et al., 2012a; Demarchi et al., 2012b; Duca and Del Frate, 2008; Licciardi and Del Frate, 2011). Data from Chinese platforms such as the HJ-1A and TG-1 (Tong et al., 2014; Guo et al., 2016) and the Russian Resurs-P fleet (Zaichko, 2014) are also promising but currently not available to the public. There are several spaceborne imaging spectrometer missions planned for the near future such as PRISMA (Guarini et al., 2017), DESIS (Mueller et al., 2017), EnMAP (Guanter et al., 2015), HyspIRI (Abrams and Hook, 2013) and HISUI (Matsunaga et al., 2014). These upcoming missions could provide data on a regular and operational basis suitable for monitoring urban functionalities.

To explore the full potential of spaceborne imaging spectrometer data in urban environments, simulated imagery has been used (e.g. Roberts et al., 2012; Okujeni et al., 2015; Rosentreter et al., 2017). These studies focus on adapting and improving mapping methods, where the majority of mapping concepts and techniques has to cope with the high spectral information content and the complex spectral mixtures (Small, 2003) that occur in the image data due to diverse material compositions and structures in the urban environment. A variety of linear and non-linear Spectral Mixture Analyses (SMA) have been developed (Shimabukuro and Smith, 1991; Keshava, 2003; Adams and Gillespie, 2006), all of which estimate abundances of surface materials within a pixel, provided that all occurring surface materials, so-called Endmembers (EM) are known (Adams et al., 1986). This concept was successfully applied to airborne imaging spectroscopy data for various environments (Adams and Smith, 1986; Asner and Lobell, 2000; Okin et al., 2001; Asner and Heidebrecht, 2002; Neville et al., 2003; Roth et al., 2012; Roberts et al., 2017). However, uncertainty in abundance estimation increases with the number of EMs in a mixing model (Winter et al., 2003). Therefore, concepts such as Multiple Endmember Spectral Mixture Analysis (MESMA) (Roberts et al., 1998) have been developed, which allows the number of EMs per pixel to be varied and optimized (e.g. Dennison and Roberts, 2003). Further, mathematical and spatial constraints have been introduced (e.g. Dennison and Roberts, 2003; Roessner et al., 2001; Rogge et al., 2006; Franke et al., 2009) to reduce the number of EMs per pixel (Zare and Ho, 2014), rather than considering all EMs occurring in a scene for generating the per-pixel mixture model. The EM variability and its influence on spectral mixture analysis have been discussed in Somers et al. (2011).

The applicability of spectral unmixing approaches for identifying surface materials using present and upcoming spaceborne imaging spectrometer systems is limited. The spatial resolution of most of these systems ranges between 20 m and 30 m. Consequently, the number of EMs per pixel usually increases and the complexity of spectral mixtures in urban areas can hardly be explained by models containing just a few EMs. Further, it is challenging to find spectrally pure EMs, which is a requirement for SMA. The latter problem was tackled by a concept developed by Okujeni et al. (2013) that uses synthetically mixed urban spectra applied to simulated EnMAP data of Berlin (Okujeni et al., 2015) using support vector regression. Sub-pixel abundances of surface categories such as roofs, pavement, low vegetation and trees could be estimated with higher accuracies in comparison to spaceborne multispectral data (Okujeni et al., 2015). However, the majority of detailed surface material related information is lost in this generalization because the mixed spectra cannot be deconvolved at this high thematic level. Improvements in mapping the broad vegetation, imperviousness and soil classes (Ridd, 1995) or extended VIS (vegetation-impervious-soil) classes (e.g. Weng et al., 2008; Okujeni et al., 2015) could be achieved by using spaceborne imaging spectroscopy data instead of multispectral imagery with the same spatial resolution.

By changing the perspective from Earth Observation (EO) images to the ground, it becomes obvious that even highly heterogeneous landscapes such as urban environments contain urban neighbourhoods with similar structural and compositional characteristics (Tobler, 1970). Often, these physical characteristics are a result of the specific land use. Industrial areas serve as an extreme example. They are often composed of large low-rise to mid-rise buildings and mainly impervious open surfaces. In contrast to industrial sites, residential areas such as detached housing developments are composed of small low-rise buildings, pervious surfaces such as gardens and exposed soils. This obvious link between land cover and land use is reflected in various urban classification systems such as the German Urban Structure Type (UST) classification (Wittig et al., 1998; Gilbert, 1994; Maier et al., 1996) that was established by urban ecologists to study urban biota. It describes urban areas as an ecosystem with biotic and abiotic components, whereby the ecosystem is formed by its history, structure and function (Sukopp and Weiler, 1988; Wittig et al., 1998; Niemela, 1999). The well-known Urban Atlas (UA) nomenclature (EEA, 2017) is built by merging CORINE and the GMES Urban Services to compare the development and structure of European cities. The UA classes mainly describe land use, which cannot easily be related to physical parameters such as those required by urban climatologists (Lefebvre, 2015). Therefore, Stewart and Oke (2012) developed the Local Climate Zone (LCZ) framework. This framework explicitly considers the physical characteristics of urban areas, such as building height and compactness, vegetation abundance, and surface material characteristics, to serve as input for urban climate models. However, this framework is also subject to land use terms, as the class LCZ 10 “Heavy industry” shows, but it reveals the link between an area's land use and its resulting land cover parameters.

In summary, all of these classification frameworks have in common that they postulate the existence of urban neighbourhoods with similar physical, compositional, structural or land use characteristics or a mixture of it. Urban neighbourhoods are hence also composed of specific surface material compositions and these compositions are represented by typical spectral mixtures in spaceborne imaging spectroscopy data. The existence of such neighbourhood-specific mixtures of surface materials have been investigated by statistical analyses of roofing materials and their occurrence in UST classes in Munich, Germany (Heiden et al., 2003, 2012; Heldens, 2010). Bochow et al. (2007) successfully used the composition of surface materials, in addition to structural and form parameters, as a proxy for updating urban biotope maps in Dresden, Germany. Finally, Earth Observation based concepts of Vegetation-Imperviousness-Soil (VIS; Ridd, 1995) and extended VIS studies could show even at a very coarse spatial scale that

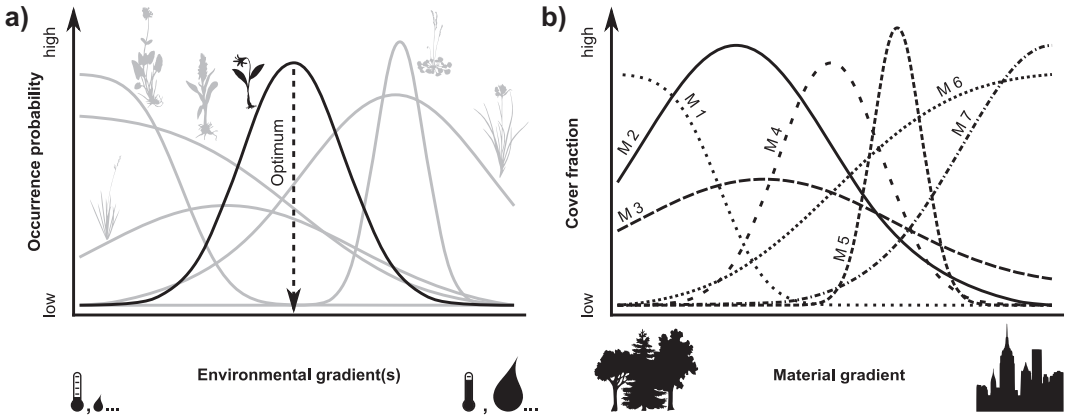

Fig. 1. a) Plant species show a maximum occurrence probability on environmental gradients (such as temperature, water, light, and nutrient availability) where the environmental conditions meet their ecological demand. However, they are able to subsist outside this optimum setting, resulting in a unimodal occurrence probability on the environmental gradient. b) Similarly, urban materials (here M1 – M7) are assumed to show a unimodal trend in their cover fractions along a non-spatial gradient in the material feature space. Co-occurrences in these distributions result in characteristic material mixtures that form gradual transitions and may be mapped with spectral data.

there are areas dominated by high albedo surfaces such as metals and concrete instead of areas that are more mixed with vegetation. The above described logic and previous work support the assumption that neighbourhood-specific surface material compositions and, thus, typical spectral mixtures are very likely to exist. Bearing in mind the drawbacks of spectral unmixing approaches, a new methodology is required to interpret the complex spectral mixtures in spaceborne imaging spectroscopy data.

A possible way to interpret complex spectral mixtures is to use gradient analysis, which so far has been used to map species compositions in natural ecosystems. We can consider the mixture of urban surface materials in analogy to the species mixture in a natural vegetation stand. Species mixtures are not arbitrary but result from the ecological demands of the individual species and gradients in the prevailing environmental conditions. Each species has an optimal, multivariate set of environmental conditions that fully meets its demands. In consequence, the highest occurrence probability of the species is given for these optimal conditions (Fig. 1a). The species is also able to subsist slightly outside its environmental optimum, but with a lower occurrence probability. In unsuitable conditions, the species will not occur. As different species have different demands, the optima of their occurrence probability curves on the environmental gradients differ, while the curves of species with similar ecological demands show some overlap. This induces a gradually changing species composition along environmental gradients in mixed vegetation stands. The concept of gradual changes in species composition in the vegetation continuum, the so-called floristic gradients, was first introduced by Gleason (1926) as an alternative to classificatory approaches. It has been successfully used in several studies for mapping vegetation as continuous fields based on remote sensing (Schmidtlein and Sassin, 2004; Schmidtlein et al., 2007; Feilhauer et al., 2011, 2014; Harris et al., 2015; Neumann et al., 2015, 2016). In the city, gradient analysis was first used by Gu et al. (2015) to quantify the composition of tree species using multi-sensor remote sensing data. Besides the fact that the resulting gradient maps preserve the fuzziness of natural vegetation patterns and, thus, provide a more accurate generalization rather than discrete classes, the approach has a fundamental advantage: The gradient concept is based on the assumption that all pixels are mixed and no “pure” pixel exists. It is, thus, not necessary to identify EMs to apply the concept. Instead, the gradients are extracted from a representative sample of mixed species compositions (Schmidtlein and Sassin, 2004). For this purpose, a gradient analysis is performed to analyse inter-correlations in the distributions of co-occurring species. The gradient analysis is basically a dimensionality reduction of the species occurrence data, where the original n dimensions of a data set with n species is reduced to a few, independent floristic gradients. It is important to note that the extracted gradients are non-spatial and only describe gradual transitions of species occurrences in the species feature space. No information on the geographical position of the samples is considered in their extraction.

In transferring this concept to mixtures of urban surface materials, we follow the hypothesis of the existence of typical surface material compositions in urban neighbourhoods, assuming that urban surface materials form patterns of co-occurring cover fractions along a non-spatial gradient in the material feature space (Fig. 1b). Here, we can assume that each surface material has a maximum in its distribution along one or multiple, non-spatial gradients and that these gradients can be extracted in a data-driven way using the gradient analysis techniques adopted from ecology. Since the approach treats all urban areas as mixtures, it may be applicable to spaceborne imaging spectroscopy data despite their rather coarse spatial resolution with complex mixed pixels. In the present proof-of-concept-study, we test whether the gradient concept offers a feasible solution for the analysis of urban data sets with a high amount of spectral mixtures. In particular, we aim to answer three questions:

- Are there gradual transitions in the occurrence of urban surface materials so that the gradient concept can be applied?
- Can these material gradients be related to spectral mixtures and can their spatial distribution be mapped with imaging spectroscopy data with 30 m spatial resolution?
- How can these spectral patterns be used to retrieve urban material compositions?

2. Study area

An area of 4.12 km^2, east of the city centre of Munich, Germany, was selected as the study site (48.133045°N, 11.565026°E and 48.106969°N, 11.631842°E). The Isar River with a broad vegetated river side, mainly east of the river, crosses through the study site from the southwest to the northeast. Further north, the large and conspicuous complex of the German Museum is located on an island. West of the Isar River, the study site is dominated by buildings originating in the Wilhelminian time, mainly built in the 19th to early 20th centuries. This part of the old town is characterized by a dense perimeter block development with a large variety of different roofing materials and marginal proportions of open space (see Fig. 2). On the eastern side of the Isar River, different USTs are alternated. The residential areas can be generally divided into perimeter and regular block development,

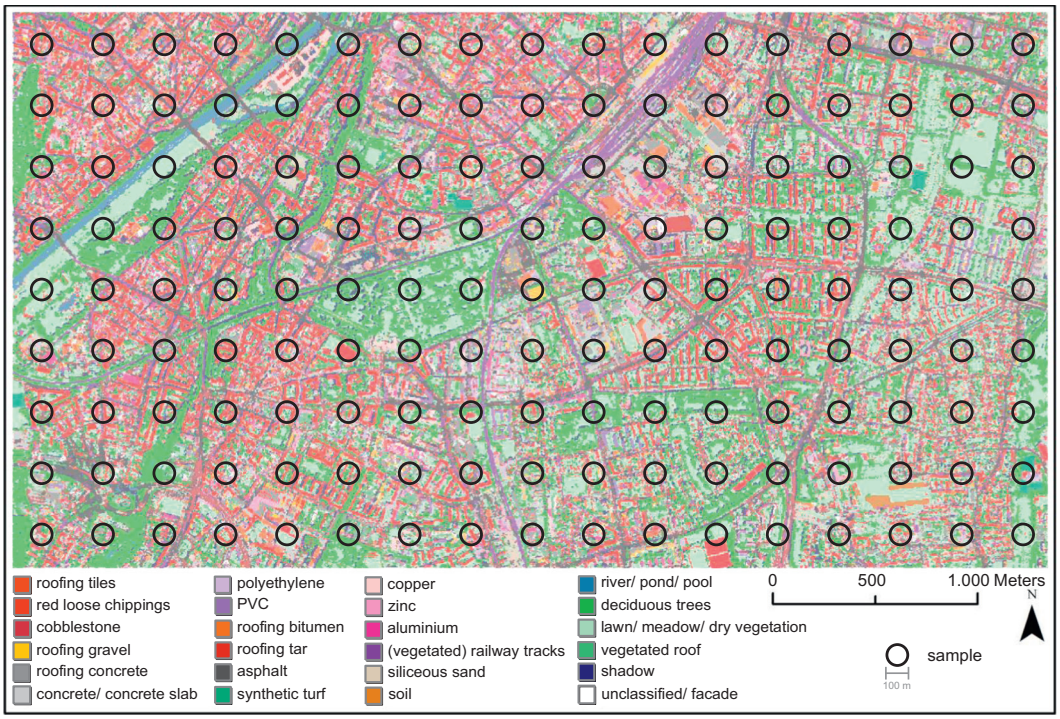

Fig. 2. Detailed urban surface material map determined from HyMap data with a systematic sampling scheme (Section 5.1) in which circles represent the sample size and position in the Munich study site. (For interpretation of the references to color in this figure legend, the reader is referred to the web version of this article.)

high-rise buildings, row house development and detached and semi-detached houses, according to the definition of UST classification in Heldens (2010). Additionally, the study site is shaped by several industrial areas with an agglomeration of differently sized halls and warehouses. The largest industrial area in the study site is located east of the railway station Ostbahnhof in the northern part. In the centre, a larger green space indicates the dimension of the eastern cemetery with a systematic combination of woody and non-woody vegetation traversed by small paths. In the southeastern part, the study site mostly consists of residential areas with detached and semi-detached houses with typically higher proportions of vegetation. For sporting and leisure purposes, several sporting fields and public parks are spread over the entire study site. In summary, USTs characterizing the study site range from residential and commercial dwellings to industrial areas, road and rail network, recreation areas such as sports fields, cemeteries, open green spaces including forested areas, and a section of the Isar River. The variety of different USTs accompanied by a wide range of predominate surface materials embedded in a relatively small-scaled area provide almost ideal preconditions for investigating urban surface material compositions and the analysis for urban gradients. For a visual representation of USTs, refer to Heldens (2010) and Heiden et al. (2012), who illustrate the differences between the individual USTs using selected examples of high-resolution orthophotos of the city of Munich.

3. Data

3.1. Airborne imaging spectroscopy data - HyMap

Imaging spectroscopy data were used for two purposes; first, as a basis for detailed surface material mapping (Heiden et al., 2012) as a surrogate for ground truth data regarding the actual material composition, and second, for simulating EnMAP reflectance of the study site. These image data were acquired with the HyMap hyperspectral sensor (Cocks et al., 1998) during the HyEurope 2007 flight campaign on June 17th and June 25th 2007 by the German Aerospace Center (DLR) Oberpfaffenhofen, Germany. Spectroscopic measurements of the study site were recorded from a flight height of 2000 m for 128 spectral bands ranging from 450 to 2500 nm, resulting in a pixel size of 4 m × 4 m. The pre-processing of the image data was carried out as described in Heldens (2010) and Heiden et al. (2012) and includes radiometric correction (Cocks et al., 1998), removal of three noisy bands, atmospheric correction, transformation into reflectance values, a nadir-normalization to correct the brightness gradient with ATCOR (Richter, 2009), geometric correction into WGS-84, UTM zone 32 N using the software ORTHO (Mueller et al., 2005), and orthorectification based on a digital terrain model produced from SRTM (Shuttle Radar Topography Mission) data (Habermeyer et al., 2008). Heldens (2010) report an average Root Mean Squared Error (RMSE) of 0.8 pixels after geometric pre-processing.

3.2. Surface material map

A detailed surface material map derived from HyMap data, with 42 initial surface material classes, served as the basis for the sampling and ordination procedure. Surface materials were identified with an automated multi-stage processing system (Heiden et al., 2012) based on the following steps: a) spectral feature-based extraction of EMs (Segl et al., 2006) using a spectral library of image spectra (Roessner et al., 2011), b) maximum likelihood classification using the previously determined EMs to increase the number of spectrally pure pixels in the image (Roessner et al., 2000; Roessner et al., 2001), c) improvement of surface material classification based on a digital surface model (DSM) obtained from a High Resolution Stereo Camera (HRSC) (Heldens, 2010) and d) iterative linear spectral unmixing to model remaining mixed pixels while considering two EMs per pixel. At 4 m HyMap resolution, almost half of the pixels correspond to pure material spectra, while the other half is composed of dominant surface material abundances. In Heldens (2010) and Heiden et al. (2012), accuracies for the surface material map were determined with an area-based approach to identify differences between the surface material map and the validation data originating from digitized building blocks using 3K aerial orthophotos. The

Table 1
Categorisation of urban surface materials (with material abbreviations) into material groups, including total and sampled cover fractions per surface material in the Munich study site.

Material Group	Surface Material	Abbreviation	Total pixels in surface material map	Sampled Cover Fractions in [%]
Minerals	roofing tiles	rtil	66,886	9.2%
	roofing concrete	rcon	27,440	7.4%
	roofing gravel	rgra	8,206	11.1%
	concrete	fcon	42,104	10.2%
	concrete slabs	pcon	11,015	8.7%
	loose chippings	prlc	20,546	10.7%
	cobblestone	pcob	47,358	8.5%
Metals	copper	rcop	13,366	8.6%
	zinc	rzin	7,607	8.0%
	aluminium	ralu	10,466	8.5%
Hydrocarbons	PVC	rpvc	13,434	8.2%
	polyethylene	rpol	8,625	9.2%
	roofing bitumen	rbit	14,883	8.3.%
	roofing tar	rtar	29,249	8.8%
	asphalt	fasp	84,854	8.1%
	synthetic turf	fkun	3,209	9.1%
Vegetation	deciduous trees	vdec	172,784	8.1%
	lawn	vlaw	16,983	8.7%
	meadow	vmea	87,525	8.9%
	dry vegetation	vdry	35,690	8.9%
	vegetated roof	rveg	18,879	8.0%
Soil and Water	siliceous sand	bsan	11,765	8.9%
	humous soil	bsoi	2,978	6.0%
	river	wriv	4,518	10.7%
	pond	wpon	4,691	8.5%
Railway tracks	railway tracks	prail	10,811	7.2%
	vegetated railway tracks	prailveg	11,546	8.1%
Total			Σ (100%) 787,418	∅ 8.7%

accuracies of surface material classes were indicated by a mean absolute error (Willmott and Matsuura, 2005) of up to 14%, with the highest underestimation of 10% occurring for the artificial material classes 'asphalt' and 'concrete' and almost 20% for the natural surface material class 'deciduous trees'. For individual accuracies of single surface material classes please refer to Heiden et al. (2012).

For simplicity and consistency reasons, several material classes were aggregated, after they were initially differentiated according to spectral intra-class variabilities, such as different coatings or according to aging effects. These material instances (e.g. old and new roofing tiles), were therefore aggregated to surface materials (e.g. roofing tiles). In addition, classes labelled as unknown, shadow or facades were removed from the surface material map, since only real surface materials that can be identified by remote sensing should be analysed with gradient analysis. The process of aggregation and removal of single material classes leads to a material map consisting of 27 surface material classes. This modified surface material map (Fig. 2) was used for the sampling (Sections 4.1 and 5.1) to analyse material compositions with gradient analysis (Section 4.2). Table 1 lists the number of pixels in the surface material map (Fig. 2) for the 27 surface material classes and the fractional abundances within the samples.

3.3. EnMAP data

The HyMap data were also used as input to simulate EnMAP reflectance values of the study site (Fig. 3) using the end-to-end simulator (Segl et al., 2012). The simulated EnMAP data are characterized by a ground sampling distance of 30 m and 242 spectral bands ranging from 423 nm to 2439 nm. Sensor specific characteristics for the prospective EnMAP mission are given in Guanter et al. (2015). In the range of the overlapping spectral bands (904 nm to 985 nm) of the two sensors (VNIR and SWIR), only the spectral bands of the SWIR sensor were used. Additional spectral bands ranging from 1358 nm to 1429 nm and 1318 nm to 1960 nm were eliminated due to atmospheric water absorption.

The samples shown in Fig. 2 (see Section 4.1), are also used for the extraction of spectral signatures and their subsequent linkage to the gradients obtained from the surface material compositions. For this purpose, the mean simulated EnMAP reflectance values of all pixels whose centre coordinates lie within a sampling polygon were calculated and used for the further analysis.

4. Methods

The complex material compositions in the urban environment are subjected to gradient analysis in order to analyse patterns of co-occurring cover fractions. Fig. 4 provides an overview of the required input data, the main processing steps (sampling, ordination, regression and prediction) and the resulting outputs from gradient analysis.

4.1. Sampling

The intention to analyse urban material compositions in simulated EnMAP pixels with gradient analysis requires a fundamental understanding of the occurrence of surface materials with regard to material-specific gradual transitions. This information can be obtained by defining samples from the surface material map (Fig. 2) with the aim to describe all occurring surface material classes and their compositions. Material compositions in the study site were analysed by means of a systematic sampling grid consisting of 153 circular polygons, each with a diameter of 100 m, evenly distributed over the study site (Fig. 2). The polygon diameter of 100 m was chosen to ensure that mixtures of materials are present in each sample and that each polygon is covered by multiple simulated EnMAP pixels. Polygons were arranged with inter-distances of 300 m between the centre points of each polygon. A systematic sampling scheme has the advantage that the urban space is sampled with a homogeneous spatial density; the inter-distances were used to mitigate effects of spatial autocorrelation in the data. Consequently, the sampling fully covers the diverse urban structures dominating the study site. Cover fractions of single surface material classes per sample were stored in a database (material table) that was finally used as input for the analysis of surface material compositions using the ordination method.

4.2. Ordination

The matrix of surface material cover fractions per polygon was passed on to a gradient analysis to extract the main gradients in surface material composition from the data. The gradient analysis arranges the sampling polygons according to their material composition in a multi-dimensional gradient space. No information on the geographic position of the sampling polygons is considered; hence, the resulting gradients are feature space gradients and not spatial gradients. Samples with similar material compositions are located nearby in the gradient space, whereas samples with very dissimilar material compositions are located on the opposing end of a gradient axis. The gradients are numbered in hierarchically decreasing order, i.e. the first gradient is the longest and most pronounced one, higher order gradients are less prominent. The position of each sample in the gradient space is indicated by a numerical score – the so-called gradient score – which is determined by the ordination in order to evaluate its similarities with respect to the composition of the material classes and their cover fractions. These gradient scores are an indicator of the surface material composition in the sample and were, therefore, used as response variables in spatial extrapolation models.

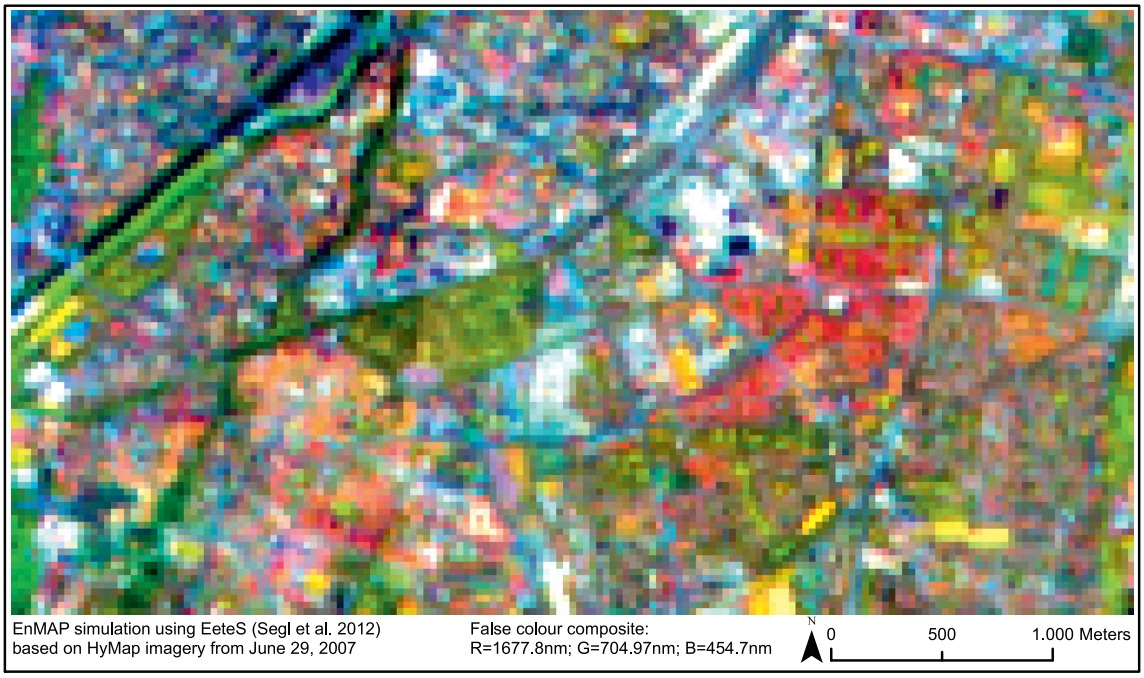

Fig. 3. Simulated EnMAP data for the Munich study site based on HyMap data. (For interpretation of the references to color in this figure legend, the reader is referred to the web version of this article.)

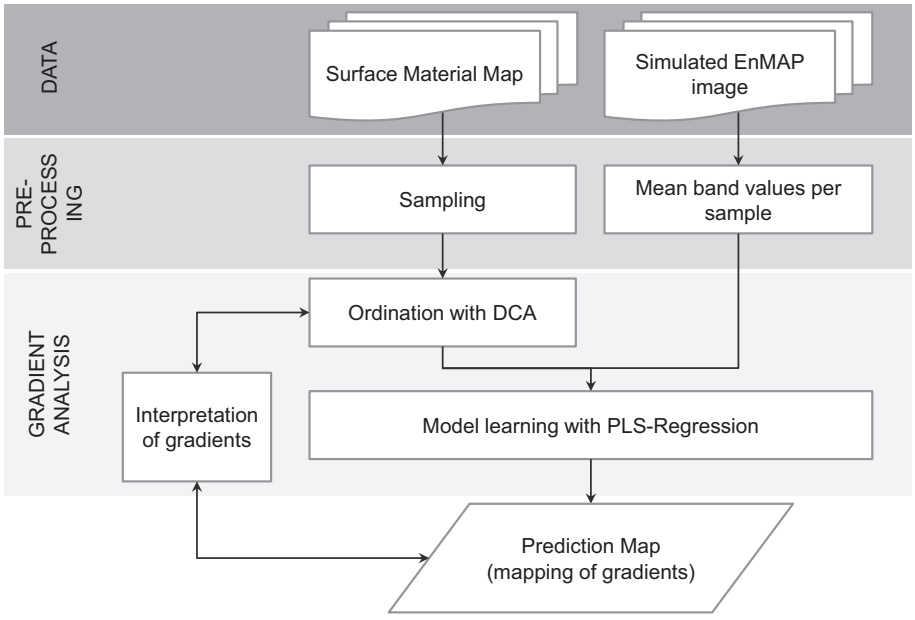

Fig. 4. Flowchart of gradient analysis for analysing material compositions in urban environments.

Several techniques can be used to perform a gradient analysis; here, we used detrended correspondence analysis (DCA; Hill and Gauch, 1980), since DCA is an established technique in vegetation science and has been successfully used for gradient mapping before (e.g. Schmidtlein and Sassin, 2004; Feilhauer and Schmidtlein, 2009; Feilhauer et al., 2011). In the present study, the selection of DCA was simply based on the authors' good experience with this technique in ecological analyses. No systematic analysis of the performance of DCA for urban gradient analysis in comparison to other techniques were conducted. In consequence, other methods for gradient analysis could have likewise been used for this pilot study. In ecology, DCA is used to model a sample distribution of varying plant species assemblages on the basis of unimodal occurrence probabilities along environmental gradients. The underlying assumption here is that species' occurrence is maximized in optimal environmental conditions. This behaviour can be determined in species samples of cover abundances that are collected over wide ranges of external gradients. For every species, a Weighted Average (WA) over all samples of cover abundances can be calculated using Gradient Values (GV) as weights. Subsequently, the samples and species are projected into a rank-ordered WA x GV matrix. The resulting matrix represents species abundances in a diagonal structure, where dissimilarities between species and gradient responses are maximized at the endpoints of the diagonal. In DCA, the gradients are not measured a priori. They start with random values and will be iteratively re-calculated until an optimal diagonal matrix is generated. Hence, the resulting GV represents a factor variable that allows for an optimal delineation of

species variance within the samples. Since one gradient often does not account for the total variance in species composition (samples with different species assemblages can be close together in a one-dimensional projection), additional axes are generated using decorrelated GVs for the iteration. The overall procedure was introduced as reciprocal averaging (Hill, 1973). In analogy to species abundances, the urban material cover can be used for the averaging cascade in order to calculate the diagonal representations of material samples within an urban gradient space. Because the gradients result from correspondence analysis, they are both unscaled and sometimes affected by artefacts. For this reason, a rescaling and detrending process was introduced in DCA. Although this correction is subject to criticism due to its mathematical inelegance (McCune et al., 2002), it is a well-performing and pragmatic technique that is frequently used in ecology. A major advantage of DCA over other algorithms for gradient analysis is the scaling of the axes in Standard Deviation (SD) units, which allows a detailed analysis of the compositional turnover in the gradient space: a distance of four SDs on a gradient indicates a full turnover, e.g. two samples with an inter-distance of four SDs have no surface materials in common (Hill and Gauch, 1980). Samples with a shorter inter-distance share at least occurrences of some materials. To mitigate an overly prominent influence of rare materials on the ordination result, we used the built-in downweighting option in our set up.

The number of gradients to be considered in the analysis is determined from the respective gradient lengths, and the percentage of total variance in the data set explained by the gradients. Short gradients that explain only a small percentage of the total variance are often very difficult to interpret, and hence, dismissed from the analysis.

4.3. Regression modelling and prediction

The gradient scores of the polygons were subsequently regressed against the averaged simulated EnMAP reflectance spectra (Section 3.3) of the corresponding pixels using Partial Least Square Regression (PLSR; Wold et al., 2001). PLSR establishes a linear relationship between the reflectance values in the spectral EnMAP bands as predictor variables and the corresponding DCA scores as response variables. A separate model is built for each DCA axis. PLSR builds the regression using latent vectors in order to handle the high degree of inter-correlation of the spectral bands, to cope with the small number of samples compared to the large number of spectral bands, and to maximize the performance of the models. These latent vectors are linear combinations of the original spectral bands that contain, on the one hand, maximum spectral information and, on the other hand, are optimized towards a good representation of the response variable. The spectral information content is hierarchically decreasing from the first to the higher order latent vectors. The number of latent vectors resulting in the smallest validation error was identified and used for the final model to minimize the risk of over-fitting. This number is determined in an elaborate procedure by analysing trends in the cross-validation RMSE. Here, we used a 10-fold cross-validation for this purpose. The importance of the individual spectral bands in the model is determined by considering the variability of the regression coefficients across the cross-validation steps (Martens and Martens, 2000). A stable and high absolute value of the coefficient in all steps of the cross-validation indicates a high importance of the spectral band for the regression. This approach allows for an efficient backward selection of spectral bands and an iterative refinement of the model towards an optimized set of spectral bands that is both parsimonious and has a strong and reliable predictive power (Schmidtlein et al., 2012). The models are finally applied to the image data for a spatial prediction of the DCA scores across the study area.

5. Results

5.1. Sampling

The sampled cover fractions of the study site are relatively similar (6%–11.1%), independent of the total coverage of the respective material classes (Table 1). The similar cover fractions of individual materials in the samples show that the sampling schema considers all materials equally, independent of their actual occurrence in the study site. Cover fractions for each surface material class per sample demonstrate the heterogeneity of material compositions in urban areas, even in these small observation units of the samples. Material compositions in the samples (Fig. 2) are formed by 4–26 different surface materials. The complexity of material compositions varies depending on the size of the urban objects and the position of the samples in the study site. Therefore, highly diverse material compositions occur more frequently in densely built-up areas of smaller objects (e.g. Wilhelminian styled urban neighbourhoods) and in industrial shaped neighbourhoods, than in relatively homogeneous areas such as open green spaces. Samples with the highest number of different surface materials are represented by block developments located in the north and in the transitional area of industrial and residential neighbourhoods in the south of the test site.

5.2. Ordination

The two main gradients determined with the DCA have an axis length of 3.1 SDs for the first gradient and 2.1 SDs for the second gradient. Samples are distributed in the material-specific DCA-space according to the determined gradient scores of the samples for both gradients (Fig. 5). The material-specific DCA-spaces visualize the differences in the occurrence of individual material classes in the sampled study site (see Table 1).

For easier interpretation of the gradients, the samples were projected onto the corresponding axis. Most material classes show a maximum occurrence along the gradients, as indicated by the position and size of the circles (Fig. 5). The left part of gradient 1 (negative DCA scores) is covered by dominant vegetation classes such as trees and meadows. The right part of gradient 1 (positive DCA scores) is mainly dominated by roofing minerals and hydrocarbons, but also by materials typically used for roads such as concrete (fcon) and asphalt (fasp). Generally, all material classes show dominant occurrence patterns along the first gradient.

Maximum occurrences for the material classes rtil, rtar, fasp, and rcop are shown along the lower (negative) part of gradient 2, while rcon, rgra, fcon, and rpol mainly occur on the upper (positive) area. Some material classes (e.g. vdec) do not have a maximum occurrence along the second gradient but occur across the entire axis with almost even cover fractions. This is also shown by the different colour hues of the samples along the second gradient. The maximum occurrences of materials can be visualized by a biplot scaling of the samples. For this purpose, material vectors were defined on the basis of the DCA scores, which determine an orientation of the occurrence of materials in the DCA-space (Fig. 6). These vectors, together with the material-specific DCA-spaces (Fig. 5), serve as a tool for interpreting the gradients.

5.3. Regression modelling

The best PLSR model for gradient 1 (Fig. 7a) resulted in $R^2 = 0.85$ for calibration and $R^2 = 0.84$ in 10-fold cross-validation. The final model was based on 35 spectral bands (distributed over the entire spectral range). These bands were selected because they survived the backward selection process and were then summarized to two latent vectors. The respective model error is indicated with an RMSE of 0.23 SDs for calibration and 0.24 SDs for validation. The model for the second gradient included five latent vectors based on 13 spectral bands

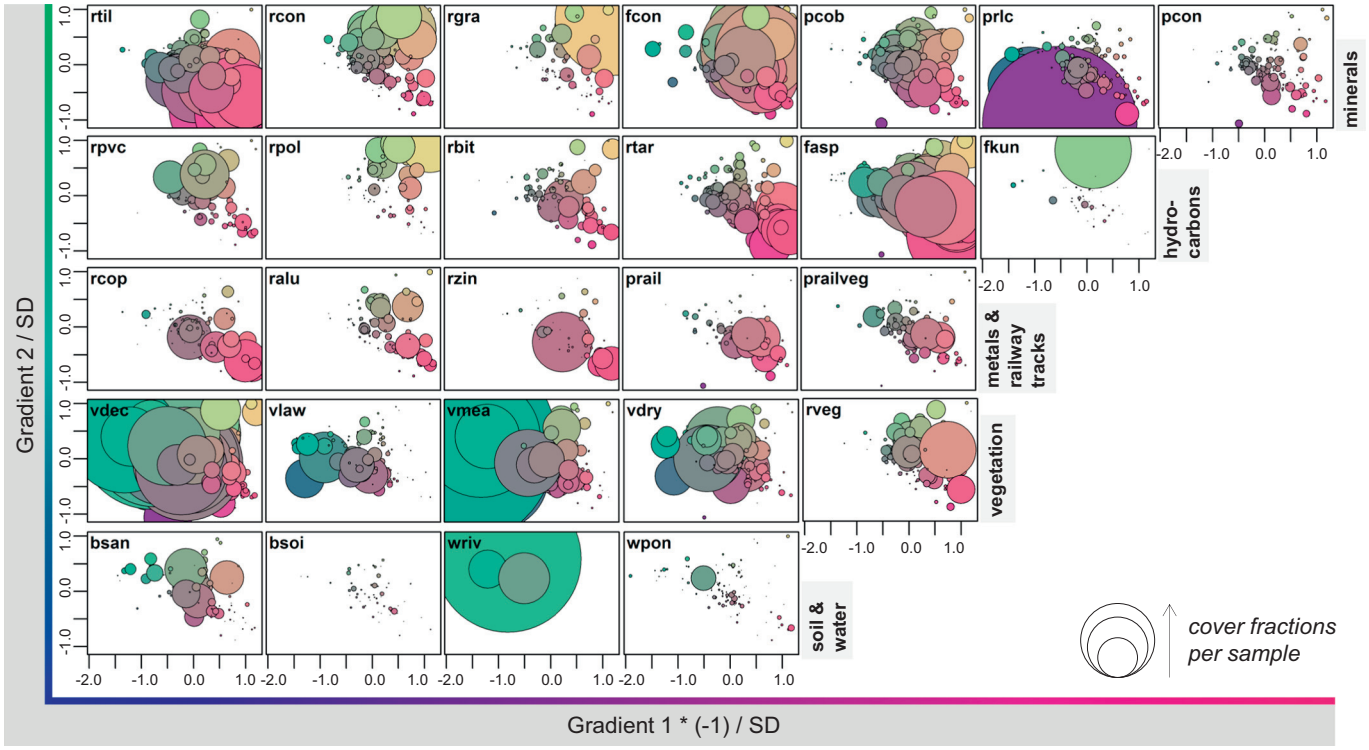

Fig. 5. Material-specific DCA-spaces facilitate the visualization of varying cover fractions in the samples to determine maximum occurrences of individual material classes. The position of a circle centre defines the position of a sample and its material composition in the DCA-space, while the circle diameter visualizes the material-specific cover fractions in each sample. The samples are coloured as a result of the transformation of the DCA-space into a colour space (see Fig. 9b). Accumulated samples indicate the maximum occurrence of this material in the gradient space. (For interpretation of the references to color in this figure legend, the reader is referred to the web version of this article.)

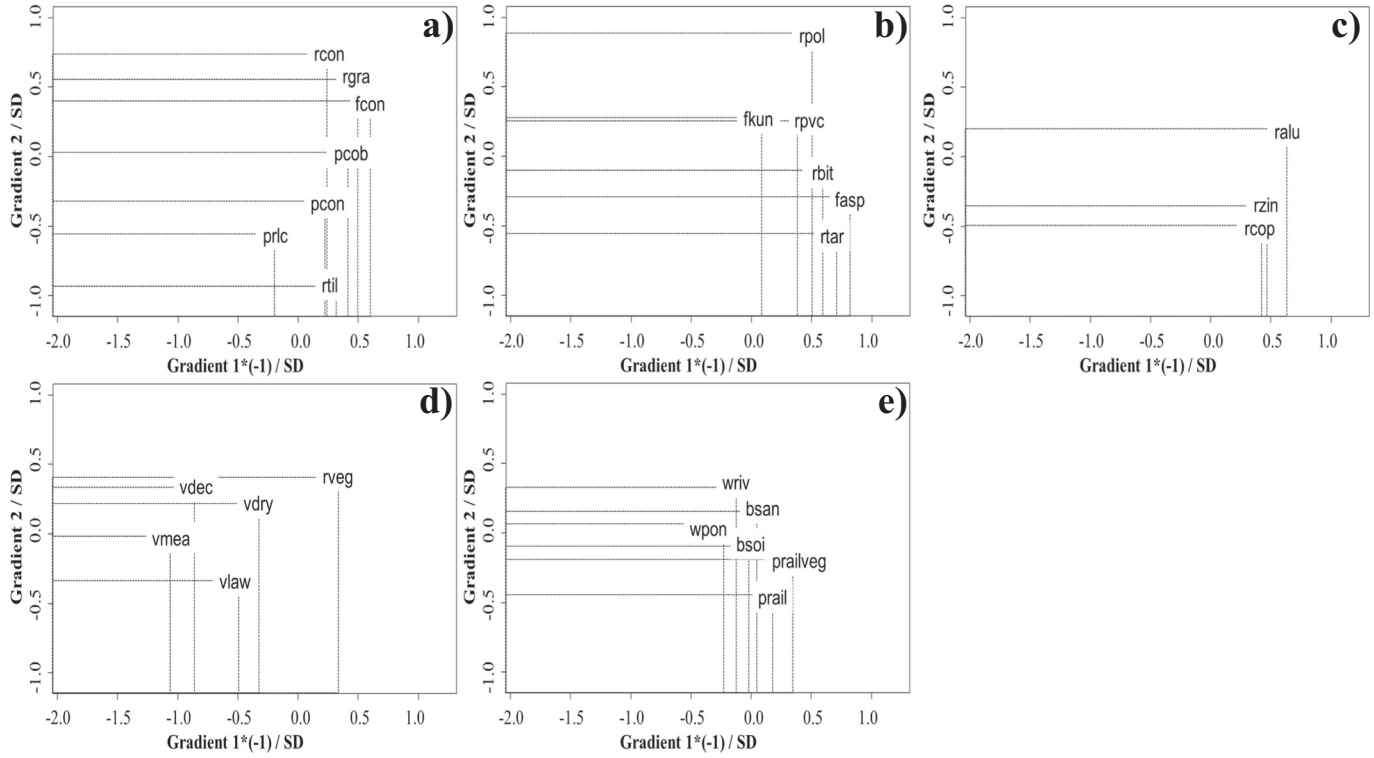

Fig. 6. Biplot scaling of the main material groups a) minerals, b) hydrocarbons, c) metals, d) vegetation, and e) the remaining material classes, composed of soil, water, and railway tracks (see Table 1), to visualize the maximum occurrences of individual material classes in the DCA-space (represented by the position of material names in the DCA-space).

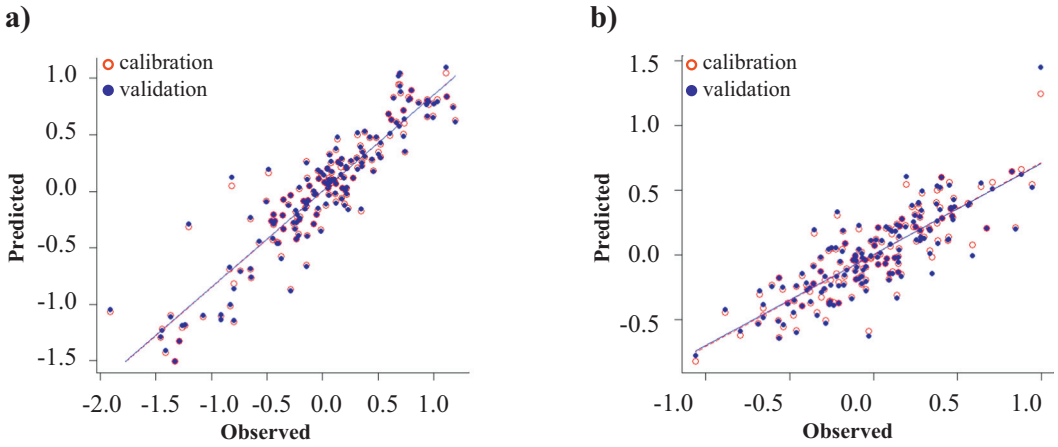

Fig. 7. Model fits of the PLS regression analysis for a) the first and b) the second gradient.

(mainly distributed in the SWIR region) with a fit of $R^2 = 0.71$ for calibration and $R^2 = 0.67$ for validation (Fig. 7b). The respective RMSE for the calibration of gradient 2 was 0.21 SDs and 0.22 SDs for validation.

5.4. Mapping of DCA scores

The regression models for the first and second gradient have been applied to the simulated EnMAP data. Pixels with predicted DCA scores exceeding ± 0.5 compared to the minimum or maximum DCA scores determined for the samples are not taken into account (white pixels), as these ranges were not covered by the sampling. A colour bar corresponding to the gradient axis is used to visualize the predicted DCA scores for gradient 1 (Fig. 8a) and gradient 2 (Fig. 8b). Fig. 8a and b show the formation of different spatial patterns based on the specific material compositions of the respective gradient, which do not coincide and, thus, give an indication of different information represented by each gradient.

The composite map in Fig. 9a combines predicted DCA scores for gradients 1 and 2, resulting in Cartesian coordinates for each pixel. The colour values of the pixels are taken from the position of the coordinates in a two-dimensional colour space (shown in Fig. 9b) that is related to the DCA-space. Accordingly, different material compositions are marked by different colour shades of the pixels in the prediction map (Fig. 9a). Similarly, coloured patterns indicate similar material compositions. Fig. 9b shows the colour scheme that is assigned to the DCA-space of both gradients with selective surface materials (written in white). The position of the surface materials in the coloured DCA-space highlights their maximum occurrence according to Fig. 6. However, similar to Fig. 9a, the colour hues need to be interpreted as surface material compositions.

The black solid and dashed boundaries in Fig. 9b results from the visual analysis and interpretation of the prediction map (Fig. 9a) that is described in detail in Section 6.2. First visual inspections indicate that the UST classification of Munich (see Section 1) widely corresponds to the patterns in the prediction map (Fig. 9a). We used this correlation to interpret the colour hues with respect to a characteristic material composition. For this purpose, we (1) selected samples from Fig. 2 that are unambiguously assigned to a specific UST using corresponding historical GoogleEarth orthophotos (Fig. 9a.I-VIII). The positions of the samples are marked by Roman numerals plotted into the prediction map. Subsequently, these samples were (2) highlighted in the colour-coded DCA-space, which leads to the formation of clusters of samples with similar material compositions. (3) Further samples are integrated into these clusters, which are adjacent to the representative samples (Fig. 9a.I-VIII) in the DCA-space, until a new assignment of samples no longer alters the UST clusters. Finally, (4) the resulting clusters were used to delineate USTs in the colour-coded DCA-space (solid and dashed lines in Fig. 9b). These cluster boundaries of USTs should not be viewed as discrete class boundaries but should characterize a probability of the occurrence of material composition that is characteristic for a certain UST. The delineated boundaries support the analysis of characteristic material compositions of USTs.

5.5. Analysing characteristic material compositions

Characteristic material compositions of USTs were analysed in order to gain an advanced understanding of typical spectral mixtures of simulated EnMAP pixels in the urban scene. For this purpose, the selected samples extracted from the sampling scheme (Fig. 2), as shown in Fig. 9a.I-VIII, were analysed for the co-occurrence of individual material classes and their cover fractions. Therefore, the material classes were aggregated to the four main material groups – minerals, metals, hydrocarbons and vegetation, according to Table 1. The material

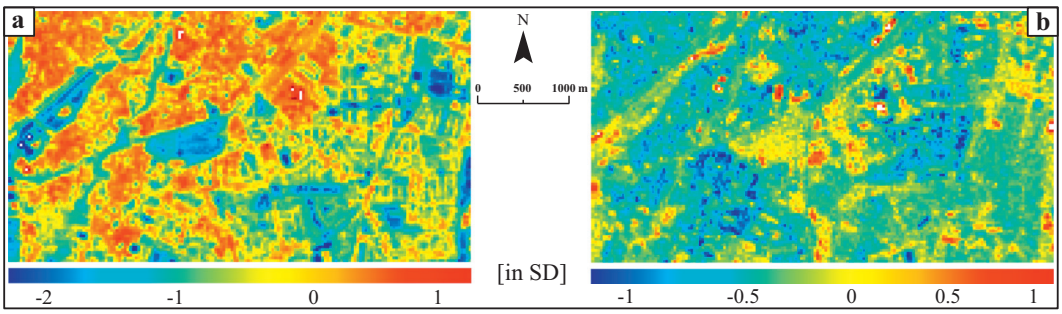

Fig. 8. Mapping of predicted DCA scores for simulated EnMAP pixels in the study site in Munich for a) the first and b) the second gradient. (For interpretation of the references to color in this figure legend, the reader is referred to the web version of this article.)

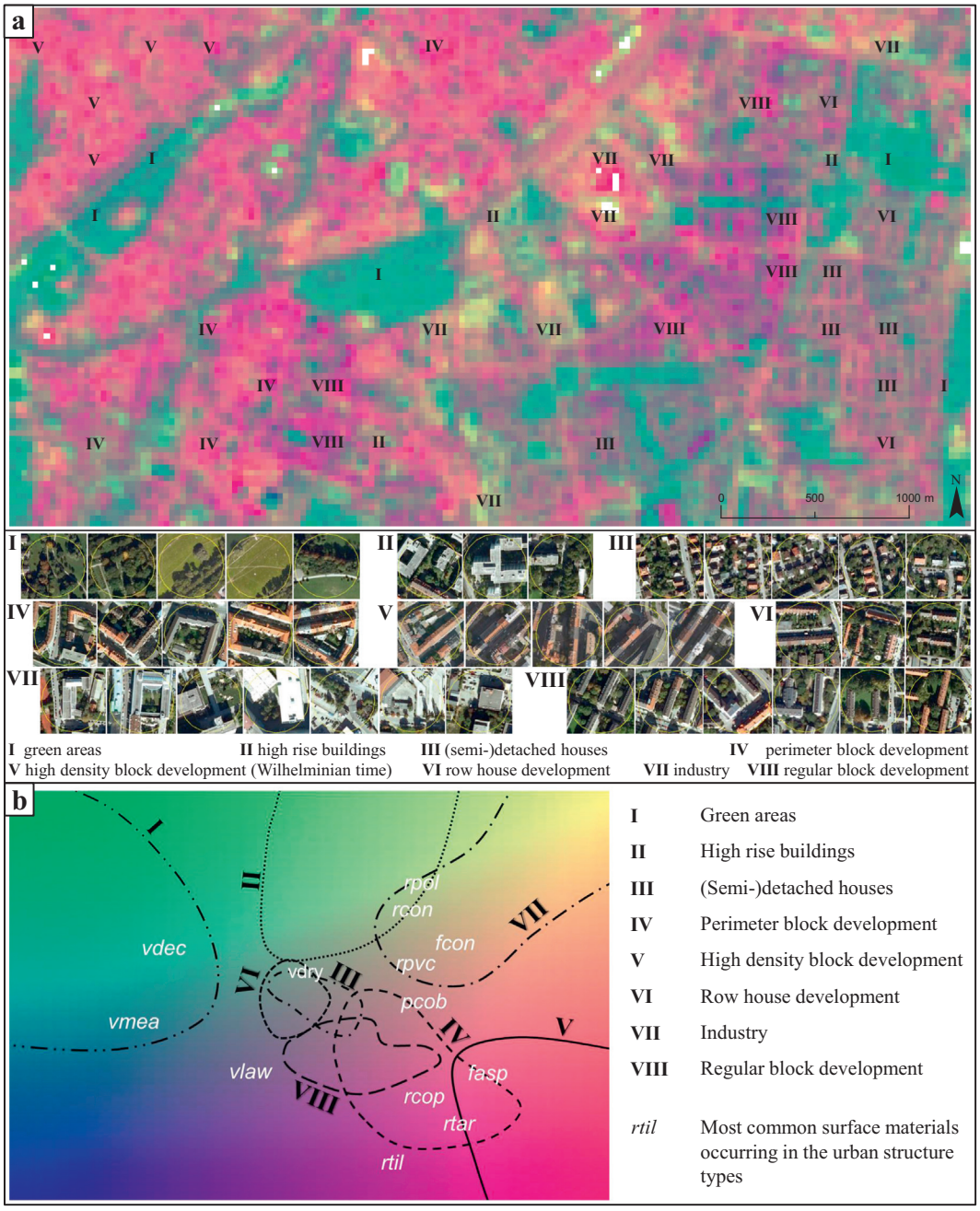

Fig. 9. a) Prediction map of DCA scores for composed gradient models for the study site in Munich, with a selection of samples from the sampling scheme (Fig. 2) that represent distinct USTs (I-VIII) - for historical high-resolution GoogleEarth® orthophotos - to support the identification of b) the colour scheme (legend) with regard to the delimitation of USTs (solid and dashed lines) based on characteristic material compositions. (For interpretation of the references to color in this figure legend, the reader is referred to the web version of this article.)

classes of soil and water were not considered, as these classes do not frequently occur in the study site, nor the urban structure railway tracks, as these are not among the observed USTs (Fig. 9a.I-VIII). Abundances of individual material classes were averaged for all samples per USTs. On the basis of these observations, the USTs are described by the most co-occurring cover fractions of dominating material classes; thus, material classes with frequencies below 5% were neglected in further analysis. Based on these statistics of averaged material cover fractions, the two most prominent material classes of each material group are displayed in Fig. 10, representing the most common surface materials for a particular UST of the study site.

6. Discussion

6.1. Do gradients exist in urban material composition?

The results in Figs. 5 and 6 demonstrate the maximum occurrence of material classes, which correspond to the theory of the probability distribution along the respective gradient axis introduced in Fig. 1. This indicates the applicability of the gradient concept for the analysis of complex material compositions in cities. The gradient interpretation is based on the analysis of dominant material distributions (determined from material-specific DCA-spaces, Fig. 5) along a corresponding gradient. On gradient 1, vegetation types mainly dominate the negative range of the DCA-space, while their cover fractions decrease towards

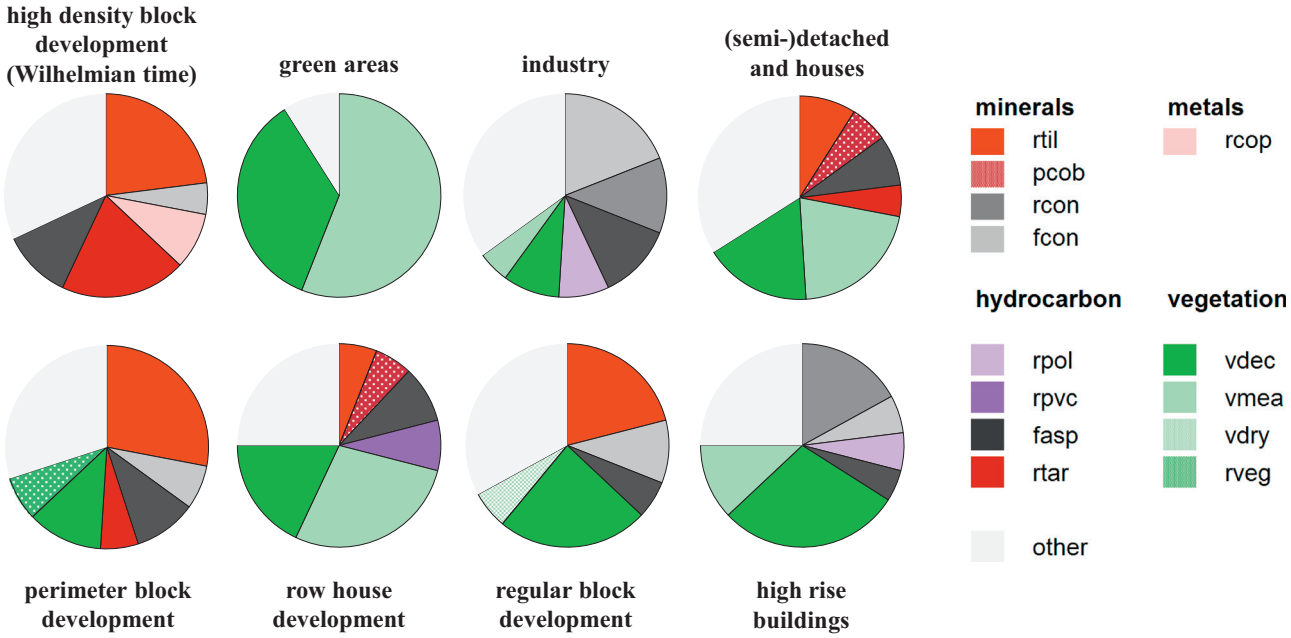

Fig. 10. Proportions (in %) of the two most commonly co-occurring material cover fractions (minimum material fraction has to be at least 5%) in the four main material groups for a selection of averaged samples per UST (Fig. 9a.I-VIII). The class 'others' comprises the remaining materials of the four main material groups as well as soil, water, and railway tracks. (For interpretation of the references to color in this figure legend, the reader is referred to the web version of this article.)

the positive end of the axis. In contrast, artificial materials such as fasp, fcon, and rbit, which are often used for rooftops and streets of larger manmade urban objects, dominate the positive end of the gradient 1 and, thus, can be interpreted as a gradient of imperviousness. The interpretation of the second gradient, with a shorter axis length, is more difficult. Artificial material groups such as minerals and hydrocarbons dominate both the negative and positive range of gradient 2. From the dominant occurrence of individual material classes along the gradient axis, possible conclusions can be drawn about land use and the functions of the built-up areas. For instance, materials that mainly occur in industrial areas have positive DCA scores on the second gradient (e.g. rcon, fcon, and rpol), while the negative DCA scores are dominated by roofing materials such as rtil, rtar and rcop, which are typically found in residential areas of European cities (Wittig et al., 1998). The maximum occurrences of individual surface materials in the samples are highlighted in the biplot scaling (Fig. 6).

The position of the materials in the biplot scaling is also important for the interpretation of the gradients. The further away the maximum occurrences of the material classes from the origin of the DCA-space (the longer the material vectors), the more reliable the prediction of the occurrence of materials. The vector length is also influenced by the frequency of material occurrences in the study site. For example, vdec is represented by 172,784 pixels (Table 1) in the study site, showing a long material vector. In contrast, bsoi, wpon and wriv have the lowest number of pixels in the study site (2978, 4691 and 4518 pixels) expressed in short material vectors. It shows that the sampling scheme is important because it represents the material abundances in the study site. Nevertheless, the dominant material occurrences and their gradual transitions show the formation of two interpretable urban gradients analogous to the formation of floristic gradients on the basis of maximum occurrences of plant species.

The visualization of the maximum occurrences of material classes along the gradient axes (Fig. 6) also indicate co-occurrences of materials. This means, for example, that in our study site, buildings covered with roofing tar (rtar) are often located in the neighbourhood of buildings with tiled roofs (rtil) and the streets are mostly asphalted (fasp), whereas, in areas with a higher occurrence of polyethylene on roofs (rpol), roofing tiles (rtil) are rarely found. These observations also confirm the neighbouring occurrence of similarly composed samples in the DCA-space. The probability of co-occurring material classes supports the assumption of the existence of typical spectral mixtures in 30 m simulated EnMAP pixels. A drawback of the wider applicability of this method could be the necessity of immense ground truth data. Since generating ground truth information can be very time- and cost-intense, if the samples are derived from field surveys or other non-automated approaches, a detailed surface material map derived from airborne imaging spectroscopy and height data is used in this study. This solid data base was necessary to prove the existence of material gradients in this study site, which is one of the major requirements to proceed with investigations about the transferability of this concept. Since transferability analysis goes far beyond the scope of this paper, it should be analysed in future studies focusing on the robustness of the gradients and the regression models.

6.2. *Are urban material gradients linked to complex spectral mixtures?*

Results of the PLS regression analysis (Fig. 7) show strong correlations between visually recognizable patterns of the simulated EnMAP reflectance and gradual transitions of materials, especially in the first gradient. The shorter length of gradient 2 led to a slightly weaker validation fit of the model compared to gradient 1. This also explains the difficulties in interpreting the second gradient (Section 6.1).

The subsequent mapping of gradient 1 on the entire simulated EnMAP image (Fig. 8a) allows the prediction of co-occurring cover fractions and their pattern formation. Fig. 8a clearly shows spatial patterns that are associated with green spaces on the one hand and built-up areas on the other hand. Based on the patterns in Fig. 8a, we observe a decrease in the proportion of vegetation coverage and, at the same time, an increase in imperviousness with increasing DCA scores. These findings are in line with the observation regarding the dominance of vegetation classes in samples with negative DCA scores on axis 1 to high cover fractions of roofing and paving materials on the opposing end of the gradient (Fig. 5). Thus, gradient 1 expresses a rural-to-urban transect (increasing urbanity from blue to red).

The prediction of gradient 2 shows new patterns (Fig. 8b) that indicate additional gradual information originating from material

occurrences. It is observed that pixels with predicted very high positive DCA scores (red) for the second gradient are dominated by a composition of material classes with typically high albedos in the VNIR range (bright material classes such as rpol), while very low predicted negative DCA scores (dark blue) correspond to material compositions of rather darker artificial materials, such as rtil. However, these findings can only be observed for the very high and very low DCA scores, while material compositions of pixels that are in the middle of the gradient space do not fully correspond to this behaviour. Thus, a dominant occurrence of materials along a brightness gradient (Small and Lu, 2006) for the second gradient axis cannot be observed. Compared to the lower DCA scores (blue), the very high DCA scores displayed in reddish shades indicate a material composition that is rather unique. These pixels were mainly composed of similar materials and characterize areas whose material composition is rarely found in the study site, such as larger sand areas or homogeneous roofs of larger storage halls. Variations in blue patterns (DCA scores ranging from −1.5 to 0) represent urban neighbourhoods with different building sizes and building orientations. Light-blue to green patterns are associated with (semi-) detached houses, while row house constructions appear in dark blue (an adjacent pattern can be observed, for example in the northeast of the study site). Mid-blue patterns are associated with perimeter block development and high-density block development (Wilhelminian time) in the southwest and northwest of the study site. Thus, the second gradient can be interpreted as a structural gradient, although no structural information was used in this study. Since the colour differences in Fig. 8 indicate different material compositions, structural differences are most probably related to a certain material composition in the simulated EnMAP pixels.

By combining the two gradients, new patterns that are associated with spectral mixtures in the simulated EnMAP data can be found. The patterns in Fig. 9a generally correspond to patterns from the surface material maps. Interpretation of the coloured patterns in terms of material compositions was carried out by visual inspections of the surface material map. As a result, patterns with a greenish shade are characterized by exceptionally high proportions of vegetation classes such as vdec and vmea. Predominantly industrially shaped regions with a significantly increased proportion of artificial materials, such as hydrocarbons, are characterized by yellowish pixels. The patterns in different shades of red characterize the various residential neighbourhoods, such as (semi-)detached houses, row houses, and block developments. Each of these is composed of a characteristic material mixture. The structural differences between the neighbourhoods described for gradient 2 (Fig. 8b) are still present in the combined prediction map. These findings are also supported by the orthophotos of different types of buildings shown in Fig. 9a.I-VIII. Therefore, we conclude that the differentiation of the structural information must indirectly result from the material compositions that determine the spectral mixtures of simulated EnMAP pixels. These findings are supported by a study of Roberts et al. (2017) that already showed the correlation between material fractions, determined with MESMA, with structural information regarding height differences in urban environments. In forests, relationships between canopy structure and leaf biochemistry were found in imaging spectroscopy data (Wang et al., 2017; Knyazikhin et al., 2013). In summary, the patterns in the combined prediction map enable a finer differentiation of the rural-to-urban transition formed by gradient 1 (Fig. 8a) and confirm the existence of co-occurring cover fractions of individual material classes in the simulated EnMAP pixels.

One might argue that a simple Tasseled Cap transformation (Crist and Kauth, 1986) of multispectral data results in a similar spatial pattern as displayed in the gradient maps. In particular, the first DCA axis with a gradual change in vegetation cover resembles the greenness component, while only the extremes of the second DCA axis corresponds to the brightness component; however, the interpretability of a Tasseled Cap transformed image is largely limited to increases in brightness and greenness, whereas the DCA-space enables more detailed conclusions. This includes the opportunity to draw pixelwise conclusions on the occurrence probability of specific materials based on their distributions in the DCA space (Fig. 5) and the ability to quantify the spatial turnover and functional diversity of materials along the gradients (see, e.g., Feilhauer and Schmidtlein, 2009 and Rocchini et al., 2018 for similar analyses targeting vegetation patterns). Neither of this is possible with a Tasseled Cap transformed multispectral image. We thus consider the additional effort required by the application of the gradient concept as justified by the additional information provided.

6.3. Do spectral patterns correspond to characteristic material compositions?

The interpretation of gradients discussed above and the patterns in the prediction map of DCA scores (Fig. 9a) for the composed gradient models (Section 6.2) can be related to the patterns of the main USTs classification of the study site based on their material compositions. The selected samples of USTs (Fig. 9a.I-VIII) were analysed in regard to their dominating material cover fractions in order to specify their characteristic material compositions. Fig. 10 shows that material compositions are distinctive for all of the selected samples.

Even in visually similar USTs such as row houses and (semi-) detached houses, the characteristic material compositions vary, especially in the occurrence of different types of hydrocarbons. The findings are in line with the formation of patterns in the mapping of the second gradient (Fig. 8b). The patterns visualize the structural differences of the USTs resulting from the different material compositions (Roberts et al., 2017) and, thus, enable their differentiation. In contrast, the USTs high-rise buildings and industry manifest the composition of the same co-occurring materials, but with varying cover fractions of material classes and also different proportions of remaining material classes. The similar material composition of the most commonly co-occurring material classes is also observable by the narrow positions of the two USTs in the legend (Fig. 9b) and verifies the difficulties in the discrimination of these two types in the prediction map. This may also be due to the fact that high-rise buildings are rather underrepresented in the study site (only three samples were available). The discrimination of the two USTs could be tackled by using additional information on the building heights, which can be derived from a digital surface model. In addition, it was observed that the samples of unambiguously assignable USTs consist of at least 2/3 co-occurring cover fractions of characteristic material classes. Through its capability of linking the knowledge of typical material compositions with urban structures, gradient analyses is a powerful tool to map characteristic material compositions in 30 m imaging spectroscopy data of urban areas.

Further testing is required to answer the question whether the urban gradient space can similarly be mapped with multispectral data or whether such detailed information can only be retrieved from IS data. A first hint is given by the regression coefficients of the PLSR model for the second gradient. These coefficients (not shown here) indicate the high explanatory power of narrow wavelength regions in the SWIR for this gradient. In particular man-made materials such as metals and hydrocarbons as well as minerals show specific absorption features in these wavelength regions. Since the second gradient largely describes variation in these materials, the regression coefficients are in line with the pattern to be expected. Multispectral sensors provide only a few broad bands in the SWIR region; we thus expect that multispectral data are less suitable for modelling the second gradient.

7. Conclusion and outlook

According to our best knowledge, this is the first study that retrieves surface material compositions from simulated spaceborne imaging spectroscopy data with a spatial resolution of 30 m. A concept developed for mapping floristic gradients in natural environments was

applied to an urban test site in Munich, Germany, to explore the capability of this method to retrieve surface material compositions from 30 m simulated EnMAP data. It has been demonstrated that there are gradual changes in material compositions in urban areas and that these gradients can be related to patterns of surface reflectance of simulated EnMAP data. The predicted gradient scores for the simulated EnMAP data results in patterns of material compositions that are related to a rural-to-urban transect (gradient 1) and allow the differentiation of structural subtleties associated with urban structures (gradient 2). The first gradient ranges from fully pervious materials, such as different vegetated surfaces, water bodies and open soils, to fully impervious materials such as roofing materials, concrete and asphalt pavements and metals. Although the second gradient is not as pronounced as the first gradient, it contains information about material related structural subtleties that can be linked to the use and function of built-up areas. A brightness gradient as, for example, described in Small and Lu (2006) could not be clearly observed in both gradients.

It is, however, important to note that DCA and, thus, also the gradient approach used in this study are data-driven and the extracted gradients are not simply transferable to other urban environments. The gradient analysis only considers materials that are included in the training dataset. Due to this fundamental constraint, the DCA-space only describes gradual transitions in the material composition of Munich. Any other urban environment may comprise new materials that are not represented by the Munich dataset. The Munich gradients are most likely not fully suitable to describe these environments, and customized gradients have to be determined from a local training dataset. However, this opens up the potential for further investigations. Since the underlying approach is data-driven, the robustness of the identified gradients needs to be tested. The consideration of a larger area of Munich, including more and possibly different urban materials, would be the first step to analyse the robustness of the gradient interpretation. Special emphasis should be placed on previously underrepresented material compositions of common urban structures (e.g. high-rise buildings) and neighbourhoods with similar material compositions such as “industry” and “high-rise buildings”.

In addition, the influence of sample size and sample distribution should be further analysed. If the polygon area is large enough to contain a mixture of different materials, the gradient analysis will always come to a result, even if the material composition does not change gradually. However, in this case, the dimensionality reduction will be rather weak and result in many short gradients that are hardly interpretable. On the other hand, if the polygon area is too small, the gradient analysis will fail to extract the gradients since the co-occurrences of materials are not adequately represented in the sampled data. In our study, the gradient analysis resulted in two long gradients that could easily be interpreted. This indicates that the polygon diameter of 100 m was sufficient for the purpose of this study. The quantity and size of the samples (Fig. 2) result in a sampling coverage of 8.6% of the total area, with the proportion of 6–11% (Table 1) for each material class regardless of its occurrence in the study area. Accordingly, natural over- or under-representations of material classes are taken into account and also confirm the suitability of the selected sampling scheme for Munich. Further research is needed to investigate the effects of the sampling scale and design on the ordination outcome. This is an important aspect to investigate the transferability of the approach to other cities.

The study presented in this paper reveals the potential for determining urban surface material compositions from data of upcoming spaceborne imaging spectroscopy missions such as EnMAP, PRISMA or HISUI. Although the pixel size of this data (30 m × 30 m) is too coarse to resolve most of the urban objects, the gradient analysis seems to be a suitable method to investigate the resulting complex spectral mixtures. The advantage of using the gradient analysis is that 1) no pure EMs are required and 2) material compositions and material co-occurrences can be retrieved that go beyond VIS or extended VIS categories. Thus, spaceborne imaging spectroscopy data could be a valuable and complementary data source for urban studies where surface material information are essential such as for urban climate modelling, urban physical modelling and for sustainable urban planning. The design of the presented study and the achieved insights build an important fundament for future analyses that will explore the extent and conditions to which the gradient concept can be transferred to unknown urban areas.

Acknowledgements

The authors would like to thank the German Aerospace Center e.V. (DLR) – Space Administration, Germany, and the Ministry of Economics and Technology (BMWi), Germany, for funding the EnFusionMAP project (50 EE 1343). We would also like to thank Dr. Karl Segl from Deutsches GeoForschungsZentrum (GFZ) in Potsdam, Germany, for simulating the EnMAP data and Dr. Wieke Heldens for providing the surface material map of Munich. Furthermore we would like to thank Dr. Nicole Pinnel for final proof reading and four anonymous reviewers for their constructive comments that helped to improve the manuscript.

References

Abrams, M.J., Hook, S.J., 2013. NASA's hyperspectral infrared imager (HyspIRI). In: Kuenzer, C., Dech, S. (Eds.), Thermal Infrared Remote Sensing. Springer, New York, NY, USA, pp. 117–130.
Adams, J.B., Gillespie, A.R., 2006. Remote Sensing of Landscapes with Spectral Images: A Physical Modeling Approach. Cambridge University Press, Cambridge, UK.
Adams, J.B., Smith, M.O., 1986. Spectral mixture modeling: a new analysis of rock and soil types at the Viking Lander 1 site. J. Geophys. Res. 91 (B8), 8098–8112.
Adams, J.B., Smith, M.O., Johnson, P.E., 1986. Spectral mixture modeling: a new analysis of rock and soil types at the Viking Lander 1 site. J. Geophys. Res. 91, 8098–8112.
Alberti, M., 2005. The effects of urban patterns on ecosystem function. Int. Reg. Sci. Rev. 28, 168–192.
Alonzo, M., McFadden, J.P., Nowak, D.J., Roberts, D.A., 2016. Mapping urban forest structure and function using hyperspectral imagery and lidar data. Urban For. Urban Green. 17, 135–147.
Asner, G.P., Heidebrecht, K.B., 2002. Spectral unmixing of vegetation, soil and dry carbon cover in arid regions: comparing multispectral and hyperspectral observations. Int. J. Remote Sens. 23 (19), 3939–3958.
Asner, G.P., Lobell, D.B., 2000. A biogeophysical approach for automated SWIR unmixing of soils and vegetation. Remote Sens. Environ. 74, 99–112.
Bagan, H., Yamagata, Y., 2012. Landsat analysis of urban growth: how Tokyo became the world's largest megacity during the last 40years. Remote Sens. Environ. 127, 210–222.
Bochow, M., Segl, K., Kaufmann, H., 2007. An update system for urban biotope maps based on hyperspectral remote sensing data. In: Proceedings of 5th EARSeL Workshop on Imaging Spectroscopy, Bruges, Belgium, April 23-25.
Bruse, M., Fleer, H., 1998. Simulating surface-plant-air interactions inside urban environments with a three dimensional numerical model. Environ. Model. Softw. 13 (3–4), 373–384.
Cai, J., Huang, B., Song, Y., 2017. Using multi-source geospatial big data to identify the structure of polycentric cities. Remote Sens. Environ. 202, 210–221.
Carter, J.G., Cavan, G., Connelly, A., Guy, S., Handley, J., Kazmierczak, A., 2015. Climate change and the city: building capacity for urban adaptation. Prog. Plan. 95, 1–66.
Cavalli, R.M., Fusilli, L., Pascucci, S., Pignatti, S., Santini, F., 2008. Hyperspectral sensor data capability for retrieving complex urban land cover in comparison with multispectral data: Venice City case study (Italy). Sensors 8 (5), 3299–3320.
Chen, F., Bornstein, R., Grimmond, S., Li, J., Liang, X., Martilli, A., Miao, S., Voogt, J., Wang, Y., 2012. Research priorities in observing and modeling urban weather and climate. Bull. Am. Meteorol. Soc. 93, 1725–1728.
Cocks, T., Jenssen, A., Stewart, A., Wilson, I., Shields, T., 1998. The HyMap airborne hyperspectral sensor: the system, calibration and performance. In: Proceedings of the 1st EARSeL Workshop on Imaging Spectroscopy, Zurich, Switzerland, October 6–8, pp. 1–6.
Crist, E.P., Kauth, R.J., 1986. The tasseled cap de-mystified. Photogramm. Eng. Remote. Sens. 52 (1), 81–86.
Demarchi, L., Canters, F., Chan, J.C.-W., Van de Voorde, T., 2012a. Multiple endmember unmixing of CHRIS/Proba imagery for mapping impervious surfaces in urban and suburban environments. IEEE Trans. Geosci. Remote Sens. 50 (9), 3409–3424.
Demarchi, L., Chan, J.C.-W., Ma, J., Canters, F., 2012b. Mapping impervious surfaces from superresolution enhanced CHRIS/Proba imagery using multiple endmember unmixing. ISPRS J. Photogramm. Remote Sens. 72, 99–112.
Demarchi, L., Canters, F., Cariou, C., Licciardi, G., Chan, J.C.-W., 2014. Assessing the performance of two unsupervised dimensionality reduction techniques on hyperspectral APEX data for high resolution urban land-cover mapping. ISPRS J. Photogramm. Remote Sens. 87, 166–179.
Dennison, P.E., Roberts, D.A., 2003. Endmember selection for mapping chaparral species and fraction using multiple endmember spectral mixture analysis. Remote Sens. Environ. 41, 123–135.

Duca, R., Del Frate, F., 2008. Hyperspectral and multiangle CHRIS-PROBA images for the generation of land cover maps. IEEE Trans. Geosci. Remote Sens. 46 (10), 2857–2866.
EEA, 2017. Copernicus Land Monitoring Service – Local Component: Urban Atlas. Online. https://land.copernicus.eu/user-corner/publications/ua-flyer/view, Accessed date: 17 September 2018.
Esch, T., Heldens, W., Hirner, A., Keil, M., Marconcini, M., Roth, A., Zeidler, J., Dech, S., Strano, E., 2017. Breaking new ground in mapping human settlements from space - the global urban footprint. ISPRS J. Photogramm. Remote Sens. 134, 30–42.
Fan, F., Deng, Y., 2014. Enhancing endmember selection in multiple endmember spectral mixture analysis (MESMA) for urban impervious surface area mapping using spectral angle and spectral distance parameters. Int. J. Appl. Earth Obs. Geoinf. 33, 290–301.
Feilhauer, H., Schmidtlein, S., 2009. Mapping continuous fields of forest alpha and beta diversity. Appl. Veg. Sci. 12, 429–439.
Feilhauer, H., Faude, U., Schmidtlein, S., 2011. Combining Isomap ordination and imaging spectroscopy to map continuous floristic gradients in a heterogeneous landscape. Remote Sens. Environ. 115, 2513–2524.
Feilhauer, H., Dahlke, C., Doktor, D., Lausch, A., Schmidtlein, S., Schulz, G., Stenzel, S., 2014. Mapping the local variability of Natura 2000 habitats with remote sensing. Appl. Veg. Sci. 17, 765–779.
Franke, J., Roberts, D.A., Halligan, K., Menz, G., 2009. Hierarchical Multiple Endmember Spectral Mixture Analysis (MESMA) of hyperspectral imagery for urban environments. Remote Sens. Environ. 113 (8), 1712–1723.
Gilbert, O.L., 1994. Städtische Ökosysteme. Neumann Verlag, Radebeul, Germany.
Grimm, N.B., Faeth, S.H., Golubiewski, N.E., Redman, C.L., Wu, J., Bai, X., Briggs, J.M., 2008. Global change and the ecology of cities. Science 319 (5864), 756–760.
Gu, H., Singh, A., Townsend, P., 2015. Detection of gradients of forest composition in an urban area using imaging spectroscopy. Remote Sens. Environ. 167, 168–180.
Guanter, L., Kaufmann, H., Segl, K., Foerster, S., Rogass, C., Chabrillat, S., Kuester, T., Hollstein, A., Rossner, G., Chlebek, C., Straif, C., Fischer, S., Schrader, S., Storch, T., Heiden, U., Mueller, A., Bachmann, M., Muehl, H., Mueller, R., Habermeyer, M., Ohndorf, A., Hill, J., Buddenbaum, H., Hostert, P., Van der Linden, S., Leitão, P.J., Rabe, A., Doerffer, R., Krasemann, H., Xi, H., Mauser, W., Hank, T., Locherer, M., Rast, M., Staenz, K., Sang, B., 2015. The EnMAP spaceborne imaging spectroscopy mission for earth observation. Remote Sens. 7, 8830–8857.
Guarini, R., Loizzo, R., Longo, F., Mari, S., Scopa, T., Varacalli, G., 2017. Overview of the prisma space and ground segment and its hyperspectral products. In: IEEE Internationl Geoscience and Remote Sensing Symposium (IGARSS), Fort Worth, TX, USA, July 23–28.
Guo, H., Dou, C., Zhang, X., Han, C., Yue, X., 2016. Earth observation from the manned low earth orbit platforms. ISPRS J. Photogramm. Remote Sens. 115, 103–118.
Habermeyer, M., Marschalk, U., Roth, A., 2008. Digital elevation model database W42-a scalable system for spatial data. In: Proceedings of the ISPRS Conference, International Archives of the Photogrammetry, Remote Sensing and Spatial Information Sciences, Beijing, China, July 3-11, pp. 1253–1258.
Harris, A., Charnock, R., Lucas, R.M., 2015. Hyperspectral remote sensing of peatland floristic gradients. Remote Sens. Environ. 162 (1), 99–111.
Heiden, U., Segl, K., Roessner, S., Kaufmann, H., 2003. Ecological evaluation of urban biotope types using airborne hyperspectral HyMap data. In: Proceedings of the 2nd GRSS/ISPRS Joint Workshop on Remote Sensing and Data Fusion over Urban Areas, Berlin, Germany, May 22-23.
Heiden, U., Segl, K., Roessner, S., Kaufmann, H., 2007. Determination of robust spectral features for identification of urban surface materials in hyperspectral remote sensing data. Remote Sens. Environ. 111, 537–552.
Heiden, U., Heldens, W., Roessner, S., Segl, K., Esch, T., Mueller, A., 2012. Urban structure type characterization using hyperspectral remote sensing and height information. Landsc. Urban Plan. 105 (4), 361–375.
Heldens, W., 2010. Use of Airborne Hyperspectral Data and Height Information to Support Urban Micro Climate Characterisation (PhD thesis). University Würzburg, Germany Online. https://opus.bibliothek.uni-wuerzburg.de/opus4-wuerzburg/frontdoor/index/index/docId/4060, Accessed date: 9 March 2018.
Herold, M., Goldstein, N.C., Clarke, K.C., 2003. The spatiotemporal form of urban growth: measurement, analysis and modeling. Remote Sens. Environ. 86 (3), 286–302.
Hill, M.O., 1973. Reciprocal averaging: an eigenvector method of ordination. J. Ecol. 61, 237–249.
Hill, M.O., Gauch, H.G., 1980. Detrended correspondence analysis: an improved ordination technique. Vegetatio 42, 47–58.
Keshava, N., 2003. A survey of spectral Unmixing algorithms. Lincoln Lab. J. 14 (1), 55–78.
Knyazikhin, Y., Schull, M.A., Stenberg, P., Mottus, M., Rautiainen, M., Yang, Y., Marshak, A., Latorre Carmona, P., Kaufmann, R.K., Lewis, P., Disney, M.I., Vanderbilt, V., Davis, A.B., Baret, F., Jacquemoud, S., Lyapustin, A., Myneni, R.B., 2013. Hyperspectral remote sensing of foliar nitrogen content. Proc. Natl. Acad. Sci. U. S. A. 110 (3), E185–E192.
Lakes, T., Kim, H.-O., 2012. The urban environmental indicator “biotope area ratio” - an enhanced approach to assess and manage the urban ecosystem services using high resolution remote-sensing. Ecol. Indic. 13 (1), 93–103.
Lefebvre, A., 2015. Feasibility study about the mapping and monitoring of green linear features based on VHR satellites imagery - EEA/MDI/14/006. In: Final Report, SIRS, Villeneuve-d'Ascq, France, Online. http://land.copernicus.eu/user-corner/technical-library/study-lead-by-sirs, Accessed date: 5 September 2018.
Licciardi, G.A., Del Frate, F., 2011. Pixel unmixing in hyperspectral data by means of neural networks. IEEE Trans. Geosci. Remote Sens. 49 (11), 4163–4172.
Maier, R., Punz, W., Dörflinger, A.N., Hietz, P., Brandlhofer, M., Fussenegger, K., 1996. Ökosystem Wien - Die Subsysteme und deren Vegetationsstruktur. Verhandlungen der Zoologisch-Botanischen Gesellschaft in Wien. Zoologisch-Botanische Gesellschaft in Wien, 133, 1-26. Online. https://www.zobodat.at/pdf/VZBG_133_0001-0026.pdf, Accessed date: 5 September 2018.
Martens, H., Martens, M., 2000. Modified Jack-knife estimation of parameter uncertainty in bilinear modelling by partial least squares regression (PLSR). Food Qual. Prefer. 11, 5–16.
Matsunaga, T., Iwasaki, A., Tsuchida, S., Tanii, J., Kashimura, O., Nakamura, R., Yamamoto, H., Tachikawa, T., Rokugawa, S., 2014. Current status of Hyperspectral Imager Suite (HISUI). In: IEEE Internationl Geoscience and Remote Sensing Symposium (IGARSS), Québec, Canada, July 13–18.
McCune, B., Grace, J.B., Urban, D.L., 2002. Analysis of Ecological Communities. MjM Software Design, Gleneden Beach, OR, USA.
Mueller, R., Lehner, M., Reinartz, P., Schroeder, M., 2005. Evaluation of Spaceborne and airborne line scanner images using a generic ortho image processor. In: Proceedings of the 2005 ISPRS High Resolution Earth Imaging for Geospatial Information, Hannover, Germany, May 17–20. vol. XXXVI.
Mueller, R., Cerra, D., Carmona, E., Alonso, K., Bachmann, M., Gerasch, B., Krawczyk, H., 2017. The hyperspectral sensor DESIS on MUSES: processing and applications. In: International Symposium on Remote Sensing of Environment (ISRSE), Tshwane, South Africa, May 8-12.
Neumann, C., Weiss, G., Schmidtlein, S., Itzerott, S., Lausch, A., Doktor, D., Brell, M., 2015. Gradient-based assessment of habitat quality for spectral ecosystem monitoring. Remote Sens. 7 (3), 2871–2898.
Neumann, C., Itzerott, S., Weiss, G., Kleinschmit, B., Schmidtlein, S., 2016. Mapping multiple plant species abundance patterns - a multiobjective optimization procedure for combining reflectance spectroscopy and species ordination. Eco. Inform. 36, 61–76.
Neville, R.A., Lévesque, J., Staenz, K., Nadeau, C., Hauff, P., Borstad, G.A., 2003. Spectral unmixing of hyperspectral imagery for mineral exploration: comparison of results from SFSI and AVIRIS. Can. J. Remote. Sens. 29 (1), 99–110.
Niemela, J., 1999. Ecology and urban planning. Biodivers. Conserv. 8 (1), 119–131.
Okin, G.S., Roberts, D.A., Murray, B., Okin, W.J., 2001. Practical limits on hyperspectral vegetation discrimination in arid and semiarid environments. Remote Sens. Environ. 77, 212–225.
Okujeni, A., Van der Linden, S., Tits, L., Somers, B., Hostert, P., 2013. Support vector regression and synthetically mixed training data for quantifying urban land cover. Remote Sens. Environ. 137, 184–197.
Okujeni, A., Van der Linden, S., Hostert, P., 2015. Extending the vegetation–impervious–soil model using simulated EnMAP data and machine learning. Remote Sens. Environ. 158, 69–80.
Pesaresi, M., Ehrlich, D., Ferri, S., Florczyk, A.J., Freire, S., Halkia, M., Julea, A., Kemper, T., Soille, P., Syrris, V., 2016. Operating procedure for the production of the global human settlement layer from Landsat data of the epochs 1975, 1990, 2000, and 2014. In: Publications Office of the European Union, EUR 27741 EN, JRC Technical Report.
Priem, F., Canters, F., 2016. Synergistic use of LiDAR and APEX hyperspectral data for high resolution urban land cover mapping. Remote Sens. 8 (10), 787.
Richter, R., 2009. ATCOR 4 User Guide. DLR-German Aerospace Centre, Remote Sensing Data Centre, Oberpfaffenhofen, Germany.
Ridd, M.K., 1995. Exploring a V-I-S (vegetation-impervious surface-soil) model for urban ecosystem analysis through remote-sensing - comparative anatomy for cities. Int. J. Remote Sens. 16 (12), 2165–2185.
Roberts, D.A., Gardner, M., Church, R., Ustin, S., Scheer, G., Green, R.O., 1998. Mapping chaparral in the Santa Monica Mountains using multiple endmember spectral mixture models. Remote Sens. Environ. 65, 267–279.
Roberts, D.A., Quattrochi, D.A., Hulley, G.C., Hook, S.J., Green, R.O., 2012. Synergies between VSWIR and TIR data for the urban environment: an evaluation of the potential for the hyperspectral infrared imager (HyspIRI) decadal survey mission. Remote Sens. Environ. 117, 83–101.
Roberts, D.A., Alonzo, M., Wetherley, E., Dudley, K., Dennison, P., 2017. Multiscale analysis of urban areas using mixing models. In: Quattrochi, D.A., Wentz, E., Lam, N.S., Emerson, C.W. (Eds.), Integrating Scale in Remote Sensing and GIS. CRC press, New York, NY, USA, pp. 247–282.
Rocchini, D., Luque, S., Pettorelli, N., Bastin, L., Doktor, D., Faedi, N., Feilhauer, H., Féret, J.B., Foody, G.M., Gavish, Y., Godinho, S., Kunin, W.E., Lausch, A., Leitão, P.J., Marcantonio, M., Neteler, M., Ricotta, C., Schmidtlein, S., Vihervaara, P., Wegmann, M., Nagendra, H., 2018. Measuring β-diversity by remote sensing: a challenge for biodiversity monitoring. Methods Ecol. Evol. 9, 1787–1798.
Roessner, S., Segl, K., Heiden, U., 2000. Comparison of automated methods for identification of urban surfaces using airborne hyperspectral data of reflective and thermal wavelength ranges. In: 2nd EARSeL workshop on imaging spectroscopy, Enschede, The Netherlands, July 11-13.
Roessner, S., Segl, K., Heiden, U., Kaufmann, H., 2001. Automated differentiation of urban surfaces based on airborne hyperspectral imagery. IEEE Trans. Geosci. Remote Sens. 39 (7), 1525–1532.
Roessner, S., Segl, K., Bochow, M., Heiden, U., Heldens, W., Kaufmann, H., 2011. Potential of hyperspectral remote sensing for analyzing the urban environment. In: Yang, X. (Ed.), Urban Remote Sensing: Monitoring, Synthesis and Modeling in the Urban Environment. John Wiley and Sons Ltd., Oxford, UK, pp. 49–62.
Rogge, D.M., Rivard, B., Zhang, J., Feng, J., 2006. Iterative spectral unmixing for optimizing per-pixel endmember sets. IEEE Trans. Geosci. Remote Sens. 44 (12), 3725–3736.
Rosentreter, J., Hagensieker, R., Okujeni, A., Roscher, R., Wagner, P.D., Waske, B., 2017. Subpixel mapping of urban areas using EnMAP data and multioutput support vector regression. In: IEEE Journal of Selected Topics in Applied Earth Observations and Remote Sensing. 10(5). pp. 1938–1948.
Roth, K.L., Dennison, P.E., Roberts, D.A., 2012. Comparing endmember selection techniques for accurate mapping of plant species and land cover using imaging

spectrometer data. Remote Sens. Environ. 127, 139–152.
Schmidtlein, S., Sassin, J., 2004. Mapping continuous floristic gradients in grasslands using hyperspectral imagery. Remote Sens. Environ. 92, 126–138.
Schmidtlein, S., Zimmermann, P., Schüpferling, R., Weiß, C., 2007. Mapping the floristic continuum: ordination space position estimated from imaging spectroscopy. J. Veg. Sci. 18, 131–140.
Schmidtlein, S., Feilhauer, H., Bruelheide, H., 2012. Mapping plant strategy types using remote sensing. J. Veg. Sci. 23, 395–405.
Segl, K., Roessner, S., Heiden, U., Kaufmann, H., 2003. Fusion of spectral and shape features for identification of urban surface cover types using reflective and thermal data. ISPRS J. Photogramm. Remote Sens. 58 (1–2), 99–112.
Segl, K., Bochow, M., Roessner, S., Kaufmann, H., Heiden, U., 2006. Feature-based identification of urban endmember spectra using hyperspectral HyMap data. In: Proceedings of the 1st EARSeL Workshop of the SIG Urban Remote Sensing, Berlin, Germany, March 2-3.
Segl, K., Guanter, L., Rogass, C., Kuester, T., Roessner, S., Kaufmann, H., Sang, B., Mogulsky, V., Hofer, S., 2012. EeteS - the EnMAP end-to-end simulation tool. In: IEEE Journal of Selected Topics in Applied Earth Observations and Remote Sensing. 5(2). pp. 522–530.
Shashua-Bar, L., Tzamir, Y., Hoffman, M.E., 2004. Thermal effects of building geometry and spacing on the urban canopy layer microclimate in a hot-humid climate in summer. Int. J. Climatol. 24 (13), 1729–1742.
Shimabukuro, Y.E., Smith, J.A., 1991. The least-square mixing model to generate fraction images from remote sensing multispectral data. IEEE Trans. Geosci. Remote Sens. 29 (1), 16–20.
Small, C., 2003. High spatial resolution spectral mixture analysis of urban reflectance. Remote Sens. Environ. 88 (1–2), 170–186.
Small, C., Lu, J.W.T., 2006. Estimation and vicarious validation of urban vegetation abundance by spectral mixture analysis. Remote Sens. Environ. 100 (4), 441–456.
Somers, B., Asner, G.P., Tits, L., Coppin, P., 2011. Endmember variability in spectral mixture analysis: a review. Remote Sens. Environ. 115 (7), 1603–1616.
Stewart, I.D., Oke, T.R., 2012. Local climate zones for urban temperature studies. Bull. Am. Meteorol. Soc. 93 (12), 1879–1900.
Sukopp, H., Weiler, S., 1988. Biotope mapping and nature conservation strategies in urban areas of the Federal Republic of Germany. Landsc. Urban Plan. 15 (1–2), 39–58.
Taleghani, M., Kleerekoper, L., Tenpierik, M., van den Dobbelsteen, A.A.J.F., 2015. Outdoor thermal comfort within five different urban forms in the Netherlands. Build. Environ. 83, 65–78.
Tobler, W.R., 1970. A computer movie simulating urban growth in the Detroit region. Econ. Geogr. 46, 234–240.
Tong, Q., Xue, Y., Zhang, L., 2014. Progress in hyperspectral remote sensing science and technology in China over the past three decades. In: IEEE Journal of Selected Topics in Applied Earth Observations and Remote Sensing. 7(1). pp. 70–91.
UN, 2014. World Urbanization Prospects: The 2014 Revision, United Nations, New York, NY, USA. Online. https://esa.un.org/unpd/wup/Publications/Files/WUP2014-Report.pdf, Accessed date: 16 March 2018.
Voltersen, M., Berger, C., Hese, S., Schmullius, C., 2014. Object-based land cover mapping and comprehensive feature calculation for an automated derivation of urban structure types at block level. Remote Sens. Environ. 154, 192–201.
Wang, Z., Skidmore, A.K., Wang, T., Darvishzadeh, R., Heiden, U., Heurich, M., Latifi, H., Hearne, J., 2017. Canopy foliar nitrogen retrieved from airborne hyperspectral imagery by correcting for canopy structure effects. Int. J. Appl. Earth Obs. Geoinf. 54, 84–94.
Weng, Q., Lu, D., 2008. A sub-pixel analysis of urbanization effect on land surface temperature and its interplay with impervious surface and vegetation cover in Indianapolis, United States. Int. J. Appl. Earth Obs. 10, 68–83.
Weng, Q., Hu, X., Lu, D., 2008. Extracting impervious surfaces from medium spatial resolution multispectral and hyperspectral imagery: a comparison. Int. J. Remote Sens. 29, 3209–3232.
Willmott, C.J., Matsuura, K., 2005. Advantages of the mean absolute error (MAE) over the root mean square error (RMSE) in assessing average model performance. Clim. Res. 30, 79–82.
Winter, M.E., Lucey, P.G., Steutel, D., 2003. Examining hyperspectral unmixing error reduction due to stepwise unmixing. In: Shen, S.S., Lewis, P.E. (Eds.), Proceedings of SPIE(5093), AeroSense 2003, Algorithms and Technologies for Multispectral, Hyperspectral, and Ultraspectral Imager IX, Orlando, FL, USA, April 21-25, pp. 380–389.
Wittig, R., Sukopp, H., Klausnitzer, B., 1998. In: Sukopp, H., Wittig, R. (Eds.), Die ökologische Gliederung der Stadt. Stadtökologie, Gustav Fischer Verlag, Stuttgart, Germany, pp. 316–372.
Wold, S., Sjöström, M., Eriksson, L., 2001. PLS-regression: a basic tool of chemometrics. Chemom. Intell. Lab. Syst. 58, 109–130.
Xu, B., Gong, P., 2007. Land-use/land-cover classification with multispectral and hyperspectral EO-1 data. Photogramm. Eng. Remote. Sens. 73, 955–965.
Zaichko, V., 2014. Current status and plans for the development of the Russian space systems for earth remote sensing. In: 28th CEOS Plenary, Tromso, Norway, October 29-30.
Zare, A., Ho, K.C., 2014. Endmember variability in hyperspectral analysis: addressing spectral variability during spectral unmixing. IEEE Signal Process. Mag. 31 (1), 95–104.
Zhang, C., 2016. Multiscale quantification of urban composition from EO-1/Hyperion data using object-based spectral unmixing. Int. J. Appl. Earth Obs. Geoinf. 47, 153–162.